PPPL--2749

DE91 012307

Transport Simulations of a Density Limit in Radiation-Dominated Tokamak Discharges. II.

D. P. Stotler
Plasma Physics Laboratory
Princeton University
Princeton, New Jersey 08543

ABSTRACT

The procedures developed previously [Phys. Fluids 31, 3713 (1988)] to simulate the radiatively induced tokamak density limit are used to examine in more detail the scaling of the density limit. It is found that the maximum allowable density increases with auxiliary power and decreases with impurity concentration. However, it is demonstrated that there is little dependence of the density limit on plasma elongation. These trends are consistent with experimental results. Our previous work used coronal equilibrium impurities; the primary result of that paper was that the maximum density increases with current when peaked profiles are assumed. Here, this behavior is shown to occur with a coronal nonequilibrium impurity as well.

I. Introduction

Recent experimental discoveries[1-4] have indicated that the density limit increases with input power. Correspondingly, the emphasis on the density limit in Compact Ignition Tokamak[5] (CIT) and International Thermonuclear Experimental Reactor[3] (ITER) design work has declined somewhat. The possible benefits, however, of a high edge density for power handling[5] still indicate a need for greater understanding of radiatively dominated tokamak discharges.

Here, we use the model developed in Ref. 7 (referred to hereafter as I) to once again focus on the density limit set by radiation. The previous work dealt only with Ohmic discharges in a TFTR geometry. A simple coronal equilibrium description of the impurities was used. The primary conclusion of I was that the electron density profile has a significant impact on the limiting density; there are two different effects involved. First, since it is the density in the highly radiative edge region that is most important in calculating the total radiated power, simulations performed with centrally peaked density profiles achieve higher Murakami parameters[8] than runs with flat profiles. The second effect noted in I was that the maximum line-averaged density increased almost linearly with plasma current when peaked profiles are used, but varies only slightly with flat profiles.

As was stated in I, our model should yield a maximum density that increases with auxiliary input power; we will demonstrate this in the present work. Recent experiments on the Joint European Tokamak[1,2] (JET) have found that the density limit scales as $P_{in}^{1/2}$ (P_{in} is the total input power). Furthermore, the edge density has been determined to be a useful parameter in describing the scaling.[1,4,9] These results seem to indicate that the tokamak density limit is indeed caused by excessive impurity radiation. There is, however, some evidence of a fuelling limit[2,10] in JET. Since these results are all consistent with our model, we can have greater confidence in using it (once properly calibrated) to predict the density limit in future devices such as CIT and ITER.

In this paper, we again consider the scaling of the density limit predicted by the $1\frac{1}{2}$-D BALDUR transport code[11] given the procedures and assumptions described in I. As alluded to above, we will show that the density limit

increases with input power, although somewhat more strongly than is indicated by the JET results. We will also demonstrate that the maximum density increases with decreasing impurity concentration, as one would expect with a radiation limit. In both cases, the noted behavior can be obtained analytically by extending the calculations of I.

The dependence of the density limit on plasma elongation is much less obvious. In order to determine this, we follow a set of experiments performed on the DIII-D tokamak.[12,13] We find, as in the DIII-D experiments,[13] that there is no strong variation of the maximum density with elongation.

The current scaling described in I arises largely because the radiated power is strongly peaked in a narrow temperature interval. Hence, there is some concern as to whether or not this result is dependent upon the assumption of coronal equilibrium impurities. We show here that the scaling of I persists with non-equilibrium impurities, at least for the case of a titanium impurity.

We describe in Sec. II the changes we have made to the simulation model discussed in I. In Sec. III, we consider the question of the auxiliary power dependence of the density limit. Section IV provides a look at the scaling of the maximum density with impurity concentration, n_z/n_e. Using a DIII-D geometry,[12] we investigate the elongation dependence in Sec. V. Then, we consider the impact of a coronal non-equilibrium model for the impurities on the density limit current scaling in Sec. VI. Finally, we summarize our findings in Sec. VII.

II. Simulation Model

The equations solved by the BALDUR code and the transport coefficients used in it are given in I. Note that all of the simulations discussed here employ the anomalous inward pinch described in I and, hence, exhibit peaked density profiles.

Although the $\chi \propto 1/n_e$ transport model is reasonable for Ohmic simulations, it fails to reproduce the degraded confinement (i.e., L-mode scaling) expected with the addition of auxiliary input power P_{aux}. Consequently, we will also make use of the Singer-Ku thermal transport model[11,14] in examining the P_{aux} dependence. This model has been found to be robust and easy

to use. Since $\chi^{SK} \propto T$, it yields the feature we are most interested in, power degradation of confinement.

The auxiliary power and impurity concentration scaling studies have been carried out with the same moments equilibrium routines mentioned in I. Use of these routines, particularly in noncircular geometries, has led to some difficulty in obtaining converged equilibria. Consequently, for simplicity, the scans of plasma elongation and current discussed in Secs. V and VI have been performed using analytic expressions for the equilibrium moments. The equilibrium packages in BALDUR have since been reworked, eliminating the numerical difficulties.[15]

In order to treat nonequilibrium impurities, separate equations must be solved for each of the impurity charge states, balancing the effects of radial diffusion, ionization, recombination, as well as sources and sinks.[16] The equations used here and their original implementation in BALDUR are described in Ref. 17. Namely, for each charge state k of an impurity of atomic number Z, we have

$$\begin{aligned}\left.\frac{\partial}{\partial t}\right|_{\xi}(n_k V') \;=\; & -\frac{\partial}{\partial \xi}\Bigg[V'\langle|\nabla\xi|\rangle \\ & \qquad \left(-D_k\frac{\partial n_k}{\partial \xi}\frac{\langle|\nabla\xi|^2\rangle}{\langle|\nabla\xi|\rangle}+n_k v_k-\frac{n_k\dot{\rho}}{\rho'\langle|\nabla\xi|\rangle}\right)\Bigg] \\ & +V'\Bigg(-\frac{n_k}{\tau_{\|}}-S_k n_e n_k+S_{k-1}n_e n_{k-1} \\ & \qquad -R_k n_e n_k+R_{k+1}n_e n_{k+1}+\mathcal{D}_k\Bigg), \qquad (1)\end{aligned}$$

where n_k is the density of charge state k, S_k and R_k are the associated ionization and recombination rates, respectively, and $\mathcal{D}_{\|}$ is the local source rate. The $1/\tau_{\|}$ term represents a simple treatment of the scrape-off losses.[18] Consequently, it is nonzero only for flux surfaces intersecting a material boundary. All other notation is as in I.

We will assume that the anomalous impurity diffusivity and pinch velocity do not vary with charge state and that their values are essenitally the same as those of the hydrogenic species (as in I): $D_k \equiv D = 0.5$ m^2/sec. $v_k \equiv v = -2Dr/a^2$. We write $\tau_{\|} = \lambda^2/D$, where λ is an effective scrape-off length

chosen to be approximately the distance between the last closed flux surface and the vacuum vessel wall.[19]

Neutrals ($k = 0$) arising from recombination are in included in Eq. (1), but have a much larger (constant) diffusivity and no pinch velocity. It is convenient to distinguish these neutrals from those due to edge sources.[16] Namely, in order to enforce a particular level of recycling or impurity influx, we include a source of $k = 1$ ions associated with neutrals streaming in from the edge. A deposition profile is calculated using the background plasma parameters and then normalized to yield the desired influx of impurity ions.[16] These appear in Eq. (1) as $\mathcal{D}_k$ which is thus nonzero only for $k = 1$.

The atomic processes included in the rate equations are electron collisional excitation and ionization, radiative and dielectronic recombination, bremsstrahlung radiation, and charge exchange recombination. The rates used here have been provided by Hulse.[16] In fact, BALDUR solutions of Eq. (1) have been compared directly with those of Hulse's MIST code.[16] Good agreement of impurity density and radiation profiles has been found for both steady-state and time-dependent situations.[20]

During a time-step, the equations Eq. (1) are solved before those of the main BALDUR code.[18] The most recently computed electron density and temperature profiles are used to evaluate the various rate coefficients in Eq. (1). Once these equations are solved, the main BALDUR code is provided with the total energy loss rate due to the impurity radiation and ionization, as well as information about the impurity density and charge state distribution. The equations for the hydrogenic densities, species temperatures and poloidal field can then be solved, completing the time-step.

III. Auxiliary Power Dependence

We choose as the initial run (i.e., $P_{aux} = 0$) in this scan the one designated "03d" in I. The other simulations in the series are carried out in the same way except that auxiliary input power is added (in equal amounts) to the electrons and ions. A centrally peaked deposition profile (falling to $\sim 1/2$ of its central value at $a/4$) is assumed. As in 03d, the line-averaged electron density $\overline{n}_e$ is raised slowly in a series of steady states. The titanium concentration n_{Ti}/n_e is held constant by puffing hydrogen gas and influxing impurity ions at the

plasma edge. Once again, the density limit is defined as the point at which $T_e = 20$ eV at the $q = 2$ surface.

In Fig. 1, we show the results of calculations at $P_{aux} = 0$, 2, and 5 MW with both the $\chi \propto 1/n_e$ and the temperature-dependent Singer-Ku transport models. Note that the two models, using the original calibration coefficients,[14] give essentially the same result at $P_{aux} = 0$. The Ohmic heating power in these simulations is typically $\sim 1 - 2$ MW. Because the range of densities required in a simulation increases with P_{aux}, this scan can not be easily extended to larger values of P_{aux}. In fact, the Singer-Ku simulation at 5 MW terminates slightly below the defined density limit ($T_e \simeq 400$ eV at $q = 2$); so, this point must be viewed as a lower bound on the density limit at the 5 MW power level.

For the $\chi \propto 1/n_e$ model, the density is increasing in an offset linear fashion with P_{aux}. The scaling for the Singer-Ku model may be somewhat weaker. The best-fit lines shown in Fig. 1 are included to illustrate these dependences.

This scaling of the maximum density with P_{aux} can be obtained analytically by extending the model developed in I. To the initial power balance inside the mixing radius r_{mix}, we add a term for the auxiliary input power.

$$r\left(n_e\chi_e\frac{dT_e}{dr} + n_i\chi_i\frac{dT_i}{dr}\right)\Bigg|_{r_{mix}} = \int_0^{r_{mix}} r\,dr\,(p_{OH} + p_{aux}). \tag{2}$$

For simplicity, we will investigate only the implications of the $\chi \propto 1/n_e$ model.

As in I we assume

$$\frac{dT_e}{dr}(r > r_{mix}) \simeq -\left(\frac{T_{e0}}{a - r_{mix}}\right). \tag{3}$$

Insertion of an expression for p_{OH} then leads directly to an equation of the form

$$\alpha T_{e0} = \beta T_{e0}^{-3/2} + P_{aux}(r_{mix}), \tag{4}$$

where the first term on the right-hand side represents the Ohmic heating power and the second term denotes the auxiliary power deposited inside the mixing radius.

In calculating the radiated power, we use a simplified form of the expression given in I since we are interested only in the scaling with P_{aux}:

$$P_{rad} \simeq 2\pi^2 R L_p (r_1 - r_2) [r_1 n_e(r_1) n_z(r_1) + r_2 n_e(r_2) n_z(r_2)]. \quad (5)$$

Namely, we are taking the radiation function to be a constant (L_p) between $T_1 = T_e(r_1)$ and $T_2 = T_e(r_2)$ and zero everywhere else. Using Eqs. (27) and (30) of I, we obtain

$$P_{rad} \propto R(a - r_{mix}) \overline{n}_e^2 \frac{n_z}{n_e} q_{cyl}^p T_{e0}^{-1/\alpha_T}, \quad (6)$$

with $p \simeq 1$ for peaked density profiles. To understand this scaling of P_{rad} with T_{e0}, one must realize that the range in radius over which radiation is emitted becomes narrower as the central temperature is increased. That is, since $P_{rad} \neq 0$ only for $T_1 < T_e < T_2$, the width of the radiating layer, $r_1 - r_2$, decreases as the local gradient of T_e becomes steeper. Since the latter increases directly with T_{e0}, as in Eq. (26) of I, we arrive at an inverse scaling for the radiated power with the central temperature. For the following, we will focus only on the scaling of $\overline{n}_{e,crit}$ and T_{e0} with P_{OH} and P_{aux}; all other factors will be lumped into the constant of proportionality.

The global power balance condition for a detached plasma is

$$P_{rad} = P_{OH}(a) + P_{aux}(a). \quad (7)$$

Writing the total $P_{OH}(a)$ in terms of the Ohmic heating power integrated out to r_{mix} [i.e., $\beta T_{e0}^{-3/2}$; see Eq. (23) of I] and using Eq. (6),

$$\overline{n}_{e,crit} \propto \left[T_{e0}^{\frac{1}{\alpha_T}} P_{aux}(a) + \beta T_{e0}^{\left(\frac{1}{\alpha_T} - \frac{3}{2}\right)} \frac{P_{OH}(a)}{P_{OH}(r_{mix})} \right]^{1/2}. \quad (8)$$

Finally, we solve Eq. (4) in two different limits. At this point we neglect any differences between $[P_{aux} + P_{OH}]_{r_{mix}}$ and $[P_{aux} + P_{OH}]_a$. In the limit of $P_{aux} \ll P_{OH}$,

$$T_{e0} \simeq \left(\frac{\beta}{\alpha}\right)^{2/5} + \frac{2}{5} \frac{P_{aux}}{\alpha}, \quad (9)$$

and

$$\overline{n}_{e,crit} - \overline{n}_{e,crit}(P_{aux} = 0) \propto P_{aux}. \quad (10)$$

In the opposite limit, $P_{aux} \gg P_{OH}$,

$$T_{e0} \propto P_{aux}, \tag{11}$$

and

$$\overline{n}_{e,crit} \propto P_{aux}^{\frac{1+\alpha_T}{2\alpha_T}}. \tag{12}$$

If we take $\alpha_T = 1.4$, the exponent on P_{aux} in Eq. (12) is 0.86.

The result for the low power limit is confirmed in Fig. 1. We do not have sufficient data or a large enough range of P_{aux} to verify Eq. (12). If the thermal diffusivity [represented by α in Eq. (4)] increases with temperature, we would expect a weaker scaling than shown in Eqs. (10) and (12). Presumably, this accounts for the less than linear increase of the maximum density with P_{aux} in the Singer-Ku case (Fig. 1).

Simpler scalings have appeared in the literature; typically, they exhibit a $P_{aux}^{1/2}$ dependence.[21] The above formulas give rise to this behavior if we assume that the size of the radiating volume is independent of P_{aux}. For example, one might account for radiation only in the region between the $q = 2$ surface and the plasma edge.[21] This assumption would be inadequate in describing our simulations (or TFTR detached plasmas) since we allow the plasma edge to approach and even go through (i.e., past the "density limit") the $q = 2$ surface.

There is experimental evidence supporting the $P_{aux}^{1/2}$ scaling,[1,2,4] although some devices have reported a weaker dependence of the maximum density on auxiliary input power.[3,13] In fact, JET has proposed a scaling for the edge density[1] which is proportional to $P_{aux}^{1/2}$. Note that the present theory as well can be more easily phrased in terms of the edge rather than the average density. That is, only the edge density appears in Eq. (5); information about the density profile must be utilized in order to write expressions in terms of $\overline{n}_e$. Since the density profiles in the BALDUR simulations vary little, the edge and average densities are roughly proportional throughout these runs.

Clearly, there are effects neglected in the present model which could affect the scaling of the maximum density with P_{aux}. First, it has long been suspected that the impurity concentration in the plasma center is related to the total power flowing to the limiter or divertor surfaces. Different wall conditions in other devices could give rise to different dependencies. Second,

the density profile shape may be affected by the input power level, the fueling method and the average density; since it is the edge density that is fundamental, the introduction of such additional variation would alter expressions for $\overline{n}_{e,crit}(P_{aux})$. Third, *both* particle and energy transport may vary with input power. Finally, JET reports some indications of a fuelling limit in their high density discharges;[2,10] this could also impact the P_{aux} scaling.

IV. Impurity Concentration Dependence

The procedure used in this section is the same as in the previous one except that each of the discharges (all Ohmic) simulated will have different values of the impurity concentration. In order to include a wide range of Z_{eff}, we employ a carbon impurity in these runs. In particular, n_C/n_e varies from 0.02 - 0.15; the corresponding values of Z_{eff} are $\sim$ 1.4 - $\sim$ 5. Of course, during a particular simulation Z_{eff} changes somewhat as the temperature profile evolves. Our results are shown in Fig. 2. The best-fit line drawn drawn through the data yields a scaling

$$\overline{n}_{e,crit} \propto \left(\frac{n_C}{n_e}\right)^{-0.33}. \tag{13}$$

It can be shown from Eqs. (28) and (34) of I that

$$\begin{aligned} \overline{n}^2_{e,crit}\frac{n_z}{n_e} &\propto Z_{eff}^{\frac{2}{5}\left(\frac{\alpha_T+1}{\alpha_T}\right)}, \\ &= \left[1+\frac{n_z}{n_e}\left(\langle Z^2\rangle - \langle Z\rangle\right)\right]^{\frac{2}{5}\left(\frac{\alpha_T+1}{\alpha_T}\right)}. \end{aligned} \tag{14}$$

We now consider two limits. First, in the case of low impurity concentration, $Z_{eff} \simeq 1$,

$$\overline{n}_{e,crit} \propto \sqrt{n_e/n_z}. \tag{15}$$

In the opposite limit of high impurity concentration, $Z_{eff} \sim Z$,

$$\overline{n}_{e,crit} \propto \left(\frac{n_z}{n_e}\right)^{\left(\frac{2-3\alpha_T}{10\alpha_T}\right)} \left(\langle Z^2\rangle - \langle Z\rangle\right)^{\frac{1}{5}\left(\frac{\alpha_T+1}{\alpha_T}\right)}. \tag{16}$$

If we insert $\alpha_T = 1.4$ into this expression, we find

$$\overline{n}_{e,crit} \propto (n_z/n_e)^{-0.16}. \tag{17}$$

Fortuitously, the best-fit exponent from the simulations is midway between those of Eqs. (15) and (17).

Experimentally, it has long been known that the limiting density is reduced as the impurity concentration is increased,[1,2,10,22,23] but detailed scalings have rarely been published. The expression appearing in Ref. 21 (motivated by empirical trends) yields $\overline{n}_{e,crit} \propto (n_z/n_e)^{-1/2}$ at fixed input power. We expect, however, that the enhanced input (Ohmic) power accompanying a rise in n_z/n_e (through Z_{eff}) will offset to some extent the radiation increase, leading to a weaker scaling of the maximum density than $(n_z/n_e)^{-1/2}$. Hence, our results are not inconsistent with those of Ref. 21.

V. Elongation Dependence

The scaling of the density limit with plasma elongation is of interest to reactor design studies. Present plans for ITER and CIT specify elongations at the 95% flux surface of $\kappa \simeq 2$. Since most of the tokamak density limit database is at $\kappa < 2$, we have another variable (in addition to plasma current, size, etc.) which must be extrapolated in order to estimate the maximum density in these devices. By investigating the question with the BALDUR code, we can help to substantiate any trends apparent in the existing database.

Recent experiments[13,24] on the DIII-D tokamak[12] have attempted to address this question directly. The following simulations are based upon these experiments. The parameters held constant throughout our runs are: $R = 1.655$ m, $a = 0.625$ m, $I_p = 0.95$ MA, and $B_T = 2$ T. We will consider elongations of $\kappa = 1.1$ 1.3, 1.5, 1.7, and 2.0. The corresponding triangularities have been estimated from the equilibrium plots presented in Ref. 24; we use $\delta = 0.13$, 0.15, 0.17, 0.29, and 0.52, respectively.

Note that the elongations quoted in Refs. 13 and 24, ranging from 1.09 to 1.99, refer to the limiter-defined flux surface. The corresponding range for the 95% flux surface[13] is 1.06 - 1.56. If one were to interpret the bounding surface in the 1-1/2-D BALDUR simulations as the 95% flux surface, the range of elongations examined here would be greater than that of the DIII-D

experiments. As mentioned in Sec. II, we make use of an analytic equilibrium prescription in these simulations. This results in a flux surface elongation that is essentially constant across the minor radius.

The particle transport model includes an anomalous inward pinch, as in the above simulations, giving rise to "peaked" density profiles. Likewise, we again make use of the $\chi \propto 1/n_e$ thermal transport model. As was discovered in the work leading up to I, simulations with titanium are more well-behaved numerically than those performed with a low-Z impurity such as carbon. Hence, we assume for simplicity that the impurity is titanium in coronal equilibrium.

Each run is a sequence of steady states at successively higher densities with a constant impurity density. Namely, the volume-averaged impurity density is the same during a simulation and is furthermore the same for all simulations. The intent of this procedure is to model as closely as possible the empirical trends (i.e., one would expect Z_{eff} to drop with increasing $\overline{n}_e$). Note that the empirical density limit data of Ref. 24 were obtained in discharges which had average densities steadily increasing in time.

The results of our simulations are presented in Fig. 3; there are no indications of a systematic scaling of the density limit with elongation. The empirical data of Refs. 13 and 24 lead to the same conclusion. In our model, high q_{cyl} (high κ) discharges are clearly detached before reaching our defined disruption point; low q_{cyl} cases are only slightly detached. Similar trends are noted in the DIII-D study.[13,24] However, the importance of locked modes in the experiments indicates that additional MHD stability physics needs to be incorporated into the simulations before accurate modeling of individual shots can be performed.

The density limit database analyzed by Greenwald included some noncircular discharges,[10] although not enough to allow the elongation dependence to be clearly discerned. The resulting scaling,

$$\overline{n}_{e,crit} = \frac{I_p}{\pi a^2} \times 10^{20}\ \mathrm{m}^{-3}, \tag{18}$$

where I_p is the plasma current in mega-amperes and a is the minor radius in meters, is independent of elongation. This scaling in particular has been found to represent recent DIII-D (as well as existing DIII) data better than others that have been proposed.[13]

These pieces of empirical evidence and the results of our simulations argue against any significant dependence of the density limit on elongation. Nonetheless, we cannot completely rule out such behavior until we have obtained a more complete picture of the physical processes involved. It is possible to use the analytic model of I to obtain an expression for the elongation scaling of the density limit. The calculations are, however, much more involved than those of the previous sections and will be deferred to a subsequent paper.

VI. Current Scaling with Non-Equilibrium Impurities

The recently incorporated changes to the BALDUR code which allow us to follow the time-development of the impurity charge state distribution yield a more realistic calculation of the impurity radiation. It is not obvious that the effects which give rise to the scalings noted above and in I will persist with this more complex description of the impurities. For this reason, we have carried out simulations using procedures which are essentially identical to those leading to runs 02d, 02f, 02g, and 02h of I, but do not assume that the impurity is in coronal equilibrium.

As in I, we perform a series of runs with titanium impurity and peaked density profiles; numerical problems apparently related to the extremely nonlinear dependence of the radiation rates on T_e have prevented us from carrying out similar simulations with low-Z impurities such as carbon. Each run consists of a sequence of steady states at successively lower values of I_p and B_T (at constant $q_{cyl} \equiv 2\pi a^2 B_T/\mu_0 R I_p$). The baseline parameters are similar to those of TFTR: $R = 2.57$ m, $a = 0.82$ m, $I_p = 2.2$ MA, and $B_T = 4.7$ T: hence $q_{cyl} = 2.8$. We arrive at runs with higher q_{cyl} by increasing the initial toroidal field strength. A new point has been added at a q_{cyl} smaller ($= 2.4$) than that of the baseline case.

The results of these simulations are presented in Fig. 4. For comparison, we have included the coronal equilibrium data points from I. Overall, the nearly linear increase of the Murakami parameter with $1/q_{cyl}$ (linear increase of density with current) persists with the non-equilibrium impurity model.

There are two features of Fig. 4 worthy of closer examination. First, the linear scaling appears to falter at the largest value of q_{cyl}. This behavior

is not predicted by the theory of I. On the other hand, the "error bars" (i.e., the range of Murakami parameters over which we must interpolate to determine the critical density) at large q_{cyl} are wider than the deviation from linearity noted in Fig. 4. Hence, it is not clear that we can rule out the linear scaling at low currents. These simulations require the most computer time to carry out because of the greater radial distance the collapse must cover to reach $q = 2$. Consequently, the runs at even larger q_{cyl} required to define the scaling more clearly in the lower current region of the Hugill diagram become prohibitively expensive and difficult to carry out, particularly with the non-equilibrium impurity model. Fortunately, most reactor design efforts focus on values of $q \lesssim 3$, so that the behavior at large safety factors is somewhat less interesting.

The second curious aspect of Fig. 4 is that the nonequilibrium runs achieve larger Murakami parameters than the coronal equilibrium simulations. Under otherwise identical circumstances, one would expect the radiation from a nonequilibrium impurity to be greater.[16,25] The apparent discrepancy arises from two effects. First, the line-averaged electron density is larger in the nonequilibrium case ($\overline{n}_e = 5.3 \times 10^{19}$ m^{-3} versus 4.7×10^{19} in the coronal equilibrium run), although the density profiles inside $r = 0.82$ m are nearly identical in the two runs. Calculating the line-averaged density involves integating n_e over the entire plasma and dividing by a characteristic plasma length scale. In both cases this length is taken to be the limiter radius. Hence, there is a contribution from the scrape-off layer density in the nonequilibrium case that is not compensated for by a larger length. This accounts for most of the difference in the two values of $\overline{n}_e$. The other contributing factor is that the impurity density is slightly larger in the equilibrium case. We would expect this to lead to greater radiation and a consequently smaller critical Murakami parameter. The impurity levels in the two sets of runs were arrived at independently during the development of the simulations.

The work described in Ref. 25 indicates that at these densities ($\sim 10^{19}$ m^{-3}) and impurity confinement times ($\lesssim 1$ s), the departures from coronal equilibrium may not be significant. Hence, it is not surprising that we have obtained results close to those of I. The need for this more realistic description of the impurities would be much greater if we were attempting to match, say, the detailed time-dependence of the radiated power in an experiment

following impurity injection.

VII. Conclusions

We have examined the dependence of the tokamak density limit (as defined in I) on a number of variables. Our results can be summarized as follows. In both 1-1/2-D BALDUR transport simulations and an analytic calculation, the maximum density has been found to increase in an offset linear fashion with input power for $P_{aux} \gtrsim P_{OH}$. The scaling is expected to be weaker at higher powers. The use of a power-degrading thermal transport model also acts to reduce the dependence of the limiting density on P_{aux}. Recent data from JET[1,2] indicate that the density limit increases with input power, although with an exponent of 1/2, and that the crucial quantity is not the line-averaged density, but the density in the highly radiative edge region (as in the BALDUR simulations; see I). Other experiments show a weaker scaling.[3,4,13] Undoubtedly, variations in the plasma-wall interactions account for some of the differences in these experimental results. A more quantitative analysis of these trends would require wall physics data to be incorporated into the BALDUR code.

With regard to impurity concentration, an overall fit to the data from our simulations has yielded $\overline{n}_{e,crit} \propto (n_z/n_e)^{-0.3}$. An analytic calculation indicates that this exponent should approach -0.5 as $n_z/n_e \to 0$; a weaker scaling prevails in the opposite limit of $Z_{eff} \sim Z$. While it is widely acknowledged that the empirical density limit increases with decreasing impurity concentration,[10,22,23] no well-known scaling expressions have been published.

Our simulations do not predict a strong dependence of the density limit on plasma elongation. Essentially the same conclusion has been drawn from experiments on DIII-D.[13,24] There are no theoretical arguments to indicate whether or not this behavior is consistent with impurity radiation being the primary cause of the tokamak density limit.

In the simulations discussed in I, the maximum density increased almost linearly with plasma current for peaked density profiles and a coronal equilibrium impurity. We have found that this trend persists when we include the effects of transport on the impurity charge state distribution by incorporating the complete set of impurity rate equations into the BALDUR simulation.

The similarity of the behavior in these runs to those using coronal equilibrium leads us to conjecture that the use of flat density profiles would again give rise to a maximum density which is nearly independent of plasma current.[7]

Although we have not made attempts to model specific experimental discharges in detail and have not incorporated a great deal of physics (beyond impurity radiation) into our simulations, the trends we are finding are largely consistent with existing density limit data. We conclude that the evidence for the density limit being precipitated by excessive impurity radiation is very strong indeed. However, the importance of the edge conditions[1,5,9] in determining the amount of radiation in the plasma indicates that a more sophisticated treatment of the scrape-off layer and divertor plasma will be required to successfully model present-day experiments.[13,26] The related need for understanding the mechanisms of impurity generation and transport[6] has led to an increased level of detailed modelling of edge plasmas. Hopefully, the results of these investigations will shed further light on the origin of the density limit in tokamaks.

Acknowledgments

This work was supported by U.S. DOE Contract No. DE-AC02-76-CHO-3073.

References

[1]P-H. Rebut for the JET Team, in *Plasma Physics and Controlled Nuclear Fusion Research 1990*, Proceedings of the 13th International Conference, Washington, DC (IAEA, Vienna, 1990), paper IAEA-CN-53/A-1-2.

[2]M. Keilhacker and the JET Team, Phys. Fluids B **2**, 1291 (1990).

[3]K. McCormick, A. Hyatt, G. Kyriakakis, E. R. Müller, H. Niedermeyer, A. Stäbler, D. Thomas, N. Tsois, ASDEX- and NI-Teams, in *Proceedings of the 17th European Conference on Controlled Fusion and Plasma Physics*, Amsterdam, 1990 (European Physical Society, Petit-Lancy, Switzerland, 1990), Vol. 3, p. 1439.

[4]T. Tsunematsu, K. Borrass, S. Cohen, F. Engelmann, J. Hogan, S. Krasheninnikov, T. Mizoguchi, V. Mukhovatov, G. Pacher, H. Pacher, V. Parail, D. Post, N. A. Uckan, J. Wesley, R. Yoshino, and the participants in the ITER Conceptual Design Activities, in Ref. 1, paper IAEA-CN-53/F-3-2.

[5]R. R. Parker, G. Bateman, P. L. Colestock, H. P. Furth, R. J. Goldston, W. A. Houlberg, D. Ignat, S. Jardin, J. L. Johnson, S. Kaye, C. Kieras-Phillips, J. Manickam, D. B. Montgomery, R. Myer, M. Phillips, R. Pillsbury, N. Pomphrey, M. Porkolab, D. E. Post, P. H. Rutherford, R. Sayer, J. Schmidt, G. Sheffield, D. J. Sigmar, D. Stotler, D. Strickler, R. Thome, R. Weiner, and J. C. Wesley, in *Plasma Physics and Controlled Nuclear Fusion Research 1988*, Proceedings of 12th International Conference, Nice, France (IAEA, Vienna, 1989), Vol. 3, p. 341.; see also G. H. Neilson and the CIT Team, Bull. Am. Phys. Soc. **35**, 2105 (1990).

[6]ITER Team, *ITER Concept Definition, Vol. 1* (International Atomic Energy Agency, Vienna, 1989).

[7]D. P. Stotler, Phys. Fluids 31, 3713 (1988).

[8]M. Murakami, J. D. Callen, and L. A. Berry, Nucl. Fusion **16**, 347 (1976).

[9]A. Stäbler H. Niedermeyer, R. Loch, V. Mertens, E. R. Müller, F. X. Söldner, F. Wagner, and the ASDEX-, NI- and Pellet-Teams, in *Proceedings of the 16th European Conference on Controlled Fusion and Plasma Physics*, Venice, 1989 (European Physical Society, Petit-Lancy, Switzerland, 1989), Vol. 1, p. 23.

[10]M. Greenwald, J. Terry, S. Wolfe, S. Ejima, M. Bell, S. Kaye, and G. H. Neilson, Nucl. Fusion **28**, 2199 (1988).

[11]D. P. Stotler and G. Bateman, Fusion Technol. **15**, 12 (1989).

[12]J. L. Luxon and L. G. Davis, Fusion Technol. **8**, 441 (1985).

[13]T. Petrie, D. Hill, A. Kellman, and M. A. Mahdavi, Bull. Am. Phys. Soc. **34**, 1969 (1989).

[14]C. E. Singer, L.-P. Ku, and G. Bateman, Fusion Technol. **13**, 543 (1988).

[15]G. Bateman (private communication).

[16]R. A. Hulse, Nucl. Technol./Fusion **3**, 259 (1983).

[17]K. Lackner, K. Behringer, W. Engelhardt and R. Wunderlich, Zeitschrift f. Naturforschung **37a**, 931 (1982).

[18]C. Singer, D. Post, D. Mikkelsen, M. Redi, A. McKenney, A. Silverman, F. Seidl, P. Rutherford, R. Hawryluk, W. Langer, L. Foote, D. Heifetz, W. Houlberg, M. Hughes, R. Jensen, G. Lister, and J. Ogden, Comput. Physics Commun. **49**, 275 (1988).

[19]B. C. Stratton, R. J. Fonck, R. A. Hulse, A. T. Ramsey, J. Timberlake, P. C. Efthimion, E. Fredrickson, B. Grek, K. W. Hill, D. W. Johnson, D. K. Mansfield, H. Park, F. J. Stauffer, and G. Taylor, Nucl. Fusion **22**, 437 (1989).

[20]D. P. Stotler, R. A. Hulse, C. E. Bush, and G. Bateman, Bull. Am. Phys. Soc. **33**, 2099 (1988).

[21]D. J. Campbell, P. A. Duperrex, A. W. Edwards, R. D. Gill, C. W. Gowers, R. S. Granetz, M. Hugon, N. Lopes Cardozo, M. Malacarne, D. C. Robinson, F. C. Schüller, P. Smeulders, J. A. Snipes, P. E. Stott, G. Tonetti, B. J. D. Tubbing, A. Weller, and J. A. Wesson, in *Plasma Physics and Controlled Nuclear Fusion Research 1986,* Proceedings of the 11th International Conference, Kyoto (IAEA, Vienna, 1987), Vol. 1, p. 433.

[22]S. J. Fielding, J. Hugill, G. M. McCracken, J. W. M. Paul, R. Prentice, and P. E. Stott, Nucl. Fusion **17**, 1382 (1977).

[23]*B. Lipschultz, J. Nucl. Mater.* **145 - 147**, 15 (1987).

[24]T. Petrie, N. Brooks, A. Kellman, M. Mahdavi, T. Osborne, D. Content, and D. Hill, Bull. Am. Phys. Soc. **33**, 1965 (1988).

[25]P. G. Carolan and V. A. Piotrowicz, Plasma Phys. **25**, 1065 (1983).

[26]K. Borass, in Ref. 3, Vol. 3, p. 1393.

Figures

FIG. 1. Maximum density as a function of auxiliary input power. The solid markers represent the $\chi \propto 1/n_e$ transport model; open markers denote use of the Singer-Ku model. The lines are "best fits" to the data points.

FIG. 2. Maximum density as a function of the relative carbon concentration. The solid line is the best-fit curve, $\overline{n}_{e,max} \propto (n_C/n_e)^{-0.33}$.

FIG. 3. Maximum density as a function of the plasma elongation.

FIG. 4. Maximum Murakami parameter allowed at a given value of $1/q_{cyl}$. The solid markers are the result of a assuming nonequilibrium impurity species. The open markers are from I; I_p, B_T scans are denoted by squares, $\overline{n}_e$ scans by circles. Lines for $\overline{n}_e = B_T/Rq_{cyl}$ (solid) and $\overline{n}_e = 2B_T/Rq_{cyl}$ (dashed) are included for comparison.

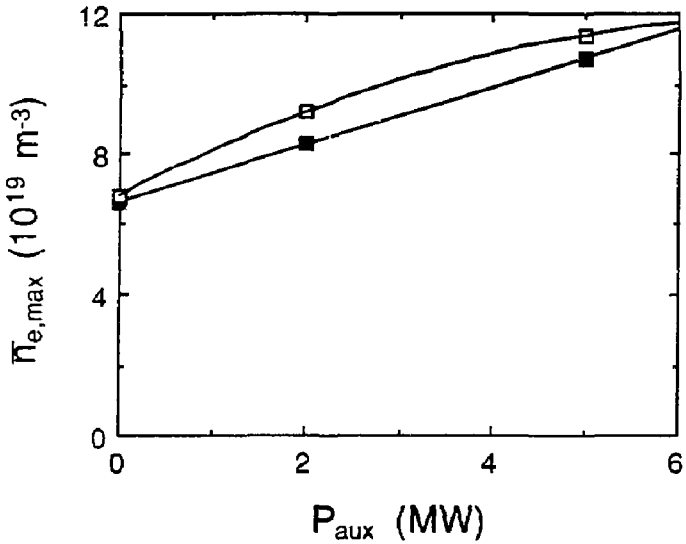

Fig. 1

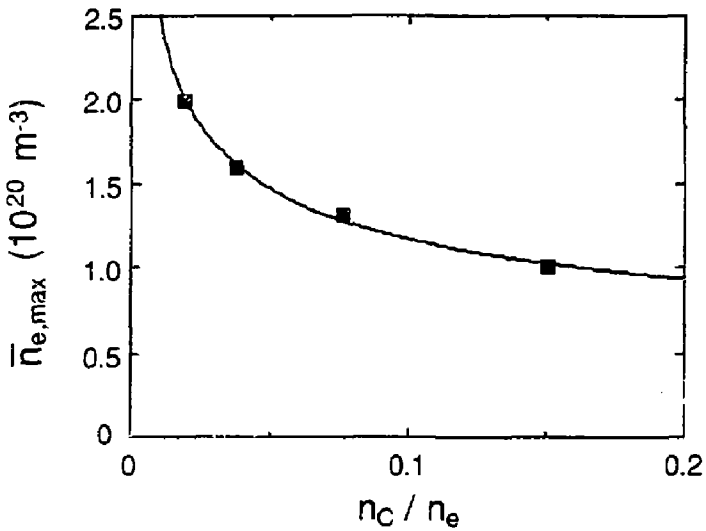

Fig. 2

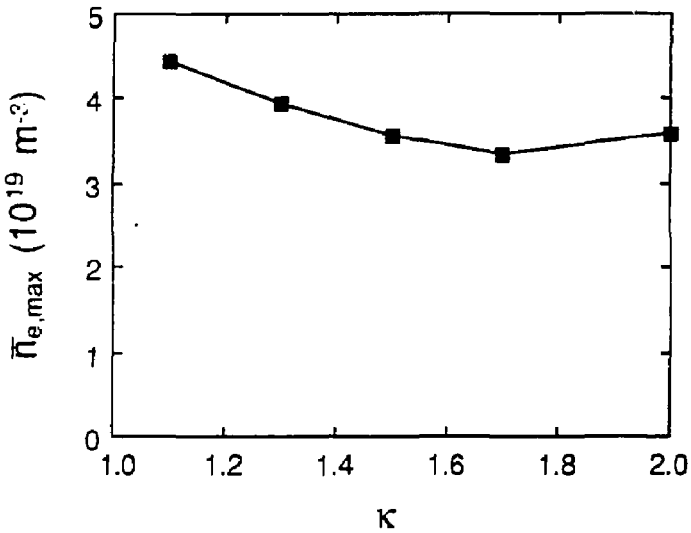

Fig. 3

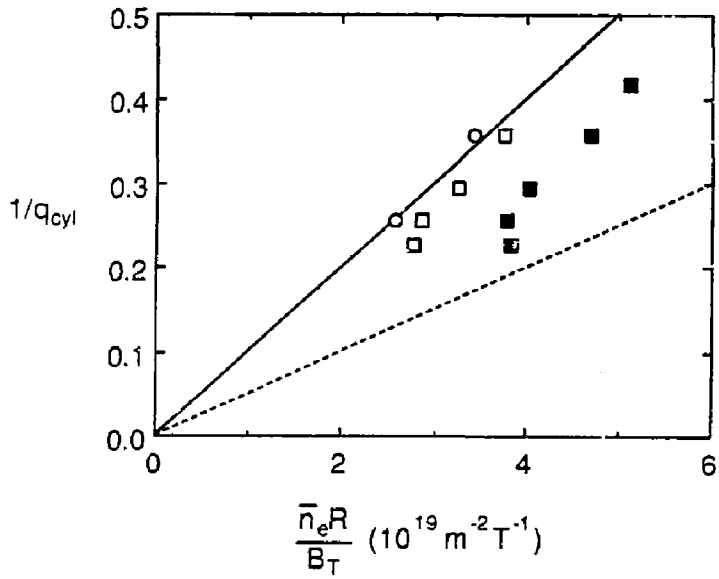

Fig. 4